



ELSEVIER

Available online at www.sciencedirect.com

SCIENCE @ DIRECT®

Ultramicroscopy 96 (2003) 17–35

ultramicroscopy

www.elsevier.com/locate/ultramic

A method for estimating the CTF in electron microscopy based on ARMA models and parameter adjustment

J.A. Velázquez-Muriel^a, C.O.S. Sorzano^a, J.J. Fernández^b, J.M. Carazo^{a,*}

^a Centro Nacional de Biotecnología, Campus Univ. Autónoma, 28049 Madrid, Spain

^b Dept. Arquitectura de Computadores y Electrónica, Univ. Almería, 04120 Almería, Spain

Received 21 February 2002; received in revised form 9 October 2002

Abstract

In this work, a powerful parametric spectral estimation technique, 2D-auto regressive moving average modeling (ARMA), has been applied to contrast transfer function (CTF) detection in electron microscopy. Parametric techniques such as auto regressive (AR) and ARMA models allow a more exact determination of the CTF than traditional methods based only on the Fourier transform of the complete image or parts of it and performing some average (periodogram averaging). Previous works revealed that AR models can be used to improve CTF estimation and the detection of its zeros. ARMA models reduce the model order and the computing time, and more interestingly, achieve increased accuracy. ARMA models are generated from electron microscopy (EM) images, and then a stepwise search algorithm is used to fit all the parameters of a theoretical CTF model in the ARMA model previously calculated. Furthermore, this adjustment is truly two-dimensional, allowing astigmatic images to be properly treated. Finally, an individual CTF can be assigned to every point of the micrograph, by means of an interpolation at the functional level, provided that a CTF has been estimated in each one of a set of local areas. The user need only know a few a priori parameters of the experimental conditions of his micrographs, for turning this technique into an automatic and very powerful tool for CTF determination, prior to CTF correction in 3D-EM.

The programs developed for the above tasks have been integrated into the X-Windows-based Microscopy Image Processing Package (Xmipp) software package, and are fully accessible at www.biocomp.cnb.uam.es.

© 2002 Elsevier Science B.V. All rights reserved.

PACS: 87.64.Dz; 07.05.Pj; 07.05.Kf; 42.30.Lr

Keywords: Electron microscopy; CTF estimation; ARMA models; Image processing; Spectral estimation

1. Introduction

Images obtained from the electron microscope are affected by many forms of aberration arising

from the complex interaction between the matter and the electron beam in the microscope. These aberrations are mainly produced by the electron source, magnetic lenses and the defocus used in experimental practice. Mathematically, the difference between a theoretical specimen projection and the actual experimental projection obtained in the micrograph is modeled by a linear

*Corresponding author. Tel.: +34-1-5854543; fax: +34-1-5854506.

E-mail address: carazo@cnb.uam.es (J.M. Carazo).

transfer function known in electron microscopy field as contrast transfer function (CTF). Although a well-established theory of image formation in transmission electron microscopy exists [1–4], that describes the CTF in parametric form, there is still a need for a good estimation method, allowing the actual shape of the CTF affecting the experimental images to be determined.

The methods used so far [5–10] include the classical spectral analysis techniques such as the periodogram (simply the square magnitude of the Fourier transform (FT) of the image) and periodogram averaging followed by a fitting of the parametric model of the CTF to a 1-D radial average of the resulting spectrum. Good results can sometimes be obtained; however, the information on the local properties throughout the micrograph is lost. In other approaches [10], the power spectrum of the image is filtered by radially limiting its inverse transform, the autocorrelation function, and then a 2-D CTF parametric fitting is done.

Previous work in our group [11] revealed that parametric spectral estimation methods, such as autoregressive (AR) models, can be used to improve the CTF estimation and the detection of its zeros. Here, an extension of this work is done using 2D-auto regressive moving average (ARMA) models [12] that allow a reduction in model order, and consequently in computing time, while also increasing estimation accuracy. Subsequently, a truly 2-D adjustment of the CTF parametric function is done, thus enabling full consideration of the CTF values (phase and amplitudes) and also the treatment of astigmatic images.

In the rest of the paper, we describe the theoretical CTF considered in our work (Section 1), discuss the methods currently used for CTF determination (Section 2), introduce ARMA models (Section 3), describe the search algorithm for the parametric CTF determination (Section 4) and the method of interpolating the CTF function to obtain local values in a micrograph (Section 5), discuss the determination of the optimal ARMA order making a comparison with the periodogram averaging method, and including results obtained for negatively stained and cryo-microscopy micrographs (Section 6), and finally,

discuss the algorithm devised and the results obtained (Section 7).

2. CTF function theory

Mathematically speaking, the image formation process in the microscope can be represented by a point spread function h that convolves the true projection ϕ of the electron density potential function of an object, yielding the experimental TEM image i :

$$i(\mathbf{r}) = h(\mathbf{r})(\phi(\mathbf{r}) + n_b(\mathbf{r})) + n_a(\mathbf{r}), \quad (1.1)$$

where \mathbf{r} is a vector in \mathbb{R}^2 representing a real space point. In Eq. (1.1), two noise terms appear. The first, n_b , denotes noise before image formation, i.e. the noise present in the projection image affected by the CTF; the second, n_a , denotes noise after image formation, i.e. the noise added by the recording and digitization processes. Fourier transformation of expression (1.1) yields

$$I(\boldsymbol{\omega}) = H(\boldsymbol{\omega})(\Phi(\boldsymbol{\omega}) + N_b(\boldsymbol{\omega})) + N_a(\boldsymbol{\omega}), \quad (1.2)$$

where $\boldsymbol{\omega}$ is a vector representing the spatial frequency, and H represents the CTF. H is a complicated parametric function, which takes into account the effects of voltage, defocus and spherical aberration of the microscope, among others.

Image formation theory states that the electrons arrive at the image plane with a phase shift $\chi(\omega)$ given by

$$\chi(\omega) = \pi\lambda(\Delta f\omega^2 + \frac{1}{2}C_s\omega^4\lambda^2). \quad (1.3)$$

Phase shift (1.3) is a function of the parameters defocus Δf , spherical aberration coefficient C_s and the wavelength of the electrons λ . When astigmatism is being considered, the size of the defocus can be expressed by its maximum Δf_M and minimum Δf_m values, which are in perpendicular directions, and the angle θ between Δf_m and the X -axis of the spatial frequency domain:

$$\begin{aligned} \Delta f(\omega) &= \text{sign}(\Delta f_M) \\ &\times \sqrt{[\Delta f_M \cos(\angle \boldsymbol{\omega} - \theta)]^2 + [\Delta f_m \sin(\angle \boldsymbol{\omega} - \theta)]^2}. \end{aligned} \quad (1.4)$$

In Eq. (1.4), $\angle \omega$ represents the angle of ω when it is expressed in polar coordinates. The mathematical expression for H , given by Erickson and Klug [1], includes both contributions of phase and amplitude contrast:

$$H(\omega) = -(\sin(\chi(\omega)) + Q(\omega)\cos(\chi(\omega))). \quad (1.5)$$

The term $Q(\omega)$ is the proportion of amplitude contrast, i.e. the fraction of electrons lost from the beam. But here a modified version is used:

$$H(\omega) = -K(\sin(\chi(\omega)) + Q(\omega)\cos(\chi(\omega))) \times E(\omega), \quad (1.6)$$

where K is a scale factor term introduced to account for discrepancies between the theoretical value given by Eq. (1.5) and the actual estimated value, and E is an attenuation term, known as envelope function [2], covering the set of effects that produce the decrease in CTF amplitude. The functional form of the attenuation term is given by

$$E(\omega) = E_{\text{spr}}(\omega)E_{\Delta f}(\omega)E_{\Delta R}(\omega)E_{\alpha}(\omega). \quad (1.7)$$

The same expression is considered in the program ICE [5], and is closely similar to those used in Ref. [8]. Below we study each of the envelope terms:

$$E_{\text{spr}}(\omega) = \exp\left[-\frac{[(\pi C_a \lambda/4)(\Delta U/V + 2\Delta I/I)]^2}{\ln(2)}\right]\omega^4. \quad (1.8)$$

This term considers the energy spread ΔU of the beam's electrons, as a percentage of the voltage V of the microscope, and the lens current instability ΔI , as a percentage of current I , and the chromatic aberration coefficient C_a .

The effect of the beam coherence is modeled by a function of its semi-angle of aperture or angular source size α :

$$E_{\alpha}(\omega) = \exp[-\pi^2 \alpha^2 (C_s \lambda^2 \omega^3 + \Delta f \omega)^2]. \quad (1.9)$$

The possible mechanical displacement ΔF , due to drifts of the sample in a direction perpendicular to the focal plane, influences the CTF by

$$E_{\Delta F}(\omega) = J_0(\pi \Delta F \lambda \omega^2), \quad (1.10)$$

where J_0 stands for the Bessel function type one and zero order. The effect of the drift ΔR in the

plane of the sample is given by Frank's formula (1969):

$$E_{\Delta R}(\omega) = \text{sinc}(\omega \Delta R). \quad (1.11)$$

The wavelength of electrons is calculated using Hall's formula (1966):

$$\lambda = \frac{1.23}{\sqrt{V + 10^{-6} V^2}} \text{ (nm)}. \quad (1.12)$$

This theoretical model has been used to adjust the CTF in our programs. The user can introduce a first estimate of the model parameters, namely V , C_a , C_s , Δf_M , Δf_m , θ , $\Delta U/V$, $\Delta I/I$, α , ΔF , ΔR , Q , as a starting point for the search algorithm, although only V and C_s are mandatory. Any of them can also be given a fixed value. It should be noted that for those combinations of parameters for which Eqs. (1.8), (1.10) and (1.11) become one and the term ω^3 in Eq. (1.9) is negligible; the general expression of Eq. (1.7) is reduced to the simpler one:

$$E(\omega) = E_{\alpha}(\omega) \approx \exp[-\pi^2 \alpha^2 (\Delta f \omega)^2] = \exp[-A\omega^2], \quad (1.13)$$

an approximation that has been adopted in previous works [7]. Indeed, in the resolution range normally used in 3D electron microscopy, where 3 or 4 CTF zeros are distinguishable, Eq. (1.13) is a sufficiently good assumption. The spherical aberration coefficient only has an important role when considering quite high spatial frequencies. Also, the effect of other parameters such as the longitudinal ΔF and horizontal ΔR displacements can be adequately included in parameter A of Eq. (1.13), thus masking the contribution of terms (1.10) and (1.11) to the general expression (1.7). The same masking effect occurs with those parameters appearing in Eq. (1.8). This means that although the model presented in Eq. (1.7) is mathematically well defined, i.e., every CTF has a defined set of parameters that cannot be altered without altering its shape, there is an entire range of parameter sets that are compatible with a given shape if one considers only a limited spatial frequency range.

In this work, we have fitted both models expressed by Eqs. (1.7) and (1.13) with good results in both cases.

3. CTF determination methods

Different methods have been applied to the problem of CTF estimation. All of them are based on spectral estimation. Given the image formation model in Eq. (1.2), its power spectrum is

$$S_I(\boldsymbol{\omega}) = |H(\boldsymbol{\omega})|^2 (S_{\Phi}(\boldsymbol{\omega}) + S_{N_b}(\boldsymbol{\omega}) + S_{N_a}(\boldsymbol{\omega})), \quad (1.14)$$

where $S_X(\boldsymbol{\omega})$ is the power spectrum of the random field X . In the case of X being a deterministic signal, $S_X(\boldsymbol{\omega})$ can be computed as $|X(\boldsymbol{\omega})|^2$.

3.1. Periodogram models

The first way of estimating the power spectrum $S_I(\boldsymbol{\omega})$ of a random field I of size $N_x \times N_y$ is the periodogram: a simple computation of the squared amplitude of the Fourier transform of the image divided by the number of pixels:

$$\hat{S}_I^{\text{PER}}(\boldsymbol{\omega}) = \frac{1}{N_x N_y} \left| \sum_{\mathbf{r}} i(\mathbf{r}) e^{-2\pi i(\boldsymbol{\omega} \cdot \mathbf{r})} \right|^2. \quad (1.15)$$

This estimator has an expected value of $S_I(\boldsymbol{\omega})$, however, its standard deviation is also $S_I(\boldsymbol{\omega})$, rendering the estimator unreliable.

An improved version of the periodogram estimator results from splitting a micrograph into k non-overlapping regions of equal size, and computing the average of the periodograms over those regions:

$$\hat{S}_I^{\text{AVPER}}(\boldsymbol{\omega}) = \frac{1}{k} \sum_k \hat{S}_{I_k}^{\text{PER}}(\boldsymbol{\omega})^2. \quad (1.16)$$

This operation reduces the variance of the estimator by a factor k , at the cost of reducing the resolution. Region overlapping may be used to achieve a stronger variance reduction [8,11]. Fernández et al. [11] obtained a mathematical expression of this reduction for the case of $K_1 \times K_2$ regions with half overlapping sections in both directions. The reduction in variance achieved by

allowing region overlap is greater since more regions inside an image can be considered. In short, these two classical estimation methods based on the Fourier transform involve a hard trade-off between spectral resolution and variance.

3.2. Autoregressive models

If the random process can be modeled as a response to a parametric system excited with some type of noise, other spectral techniques can be used that may lead to an increase in resolution. The assumption can be stated in the form of a linear difference equation for the image i :

$$i(\mathbf{x}) = \sum_{\mathbf{r} \in R} \theta_{\text{AR}}(\mathbf{r}) i(\mathbf{x} - \mathbf{r}) + \varepsilon(\mathbf{x}), \quad (1.17)$$

where ε represents the input noise that excites the system, and $\theta_{\text{AR}}(\mathbf{r})$ is a coefficient which determines how much the point $i(\mathbf{x} - \mathbf{r})$ influences the value of $i(\mathbf{x})$. R is known as the support region of the model, which indicates the region of $\mathbf{Z}^2 - \{(0, 0)\}$ used to predict the value of the current pixel. Assuming that ε is the white noise of zero mean and variance σ^2 , the corresponding model is known as AR model. The power spectrum of an image i derived from Eq. (1.17) is

$$\hat{S}_I^{\text{AR}}(\boldsymbol{\omega}) = \frac{\sigma^2}{\left| 1 - \sum_{\mathbf{r} \in R} \theta_{\text{AR}}(\mathbf{r}) e^{-2\pi i(\boldsymbol{\omega} \cdot \mathbf{r})} \right|^2}. \quad (1.18)$$

The selection of the shape and size of the support region is crucial to the performance of the AR model. According to the shape of the support region, models can be causal, semi-causal or non-causal (see Fig. 1, left, center, right). The order of the models, which determines the number of parameters considered, is given by the number of pixels in the vertical and horizontal directions. For example, a causal AR model of order (4,4) involves a support region in the non-symmetric half plane of 4 pixels considered in both directions (Fig. 1, left).

AR models with causal support regions were extensively studied in our group [11], and its usefulness was shown with real data. It was found that the greater the order of the AR model, the closer the similarity between the estimated and the actual power spectra when simulated images

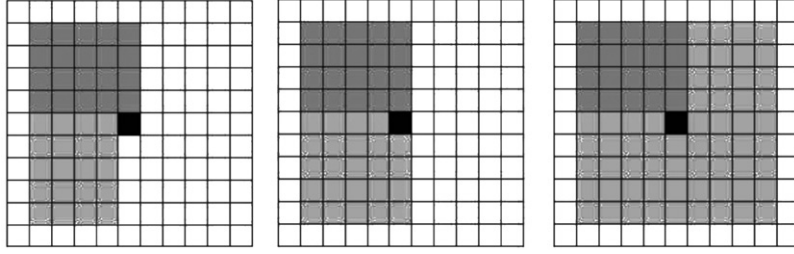


Fig. 1. Support regions for AR and ARMA models. Left: A causal region, where the value of the black pixel depends causally on both directions. Center: A semi-causal region, where the black pixel depends causally on horizontal pixels, but not causally on vertical ones, as they are unknown when the matrix is explored lexicographically. Right: A non-causal region. The black pixel depends on all its neighbors.

were used. AR models of order as high as 60×60 were used to estimate the CTF of the micrographs, thus obtaining 7320 AR coefficients.

3.3. ARMA models

In this work, we extend the use of the 2-D AR models applied to electron microscopy micrographs including moving average (MA) models in the spectral estimation technique. These models are also known as 2D-ARMA models, and here we introduce a class of them that can be used in any process with rational spectral density [12]. The difference equation that defines an ARMA model is similar to Eq. (1.17):

$$i(\mathbf{x}) = \sum_{\mathbf{r} \in R} \theta_{AR}(\mathbf{r})i(\mathbf{x} - \mathbf{r}) + \sqrt{v}\varepsilon(\mathbf{x}). \quad (1.19)$$

However, in this case the input noise term ε is correlated and does not need to be white. The term v is added recalling the variance term that appears in Eq. (1.18). The power spectrum of Eq. (1.19) is given by

$$\begin{aligned} S_I^{ARMA}(\boldsymbol{\omega}) &= \left| v \frac{1 + \sum_{\mathbf{r} \in R} \theta_{MA}(\mathbf{r})e^{-2\pi i(\boldsymbol{\omega} \cdot \mathbf{r})}}{1 - \sum_{\mathbf{r} \in R} \theta_{AR}(\mathbf{r})e^{-2\pi i(\boldsymbol{\omega} \cdot \mathbf{r})}} \right|^2 \\ &= \left| v \frac{B(\boldsymbol{\omega})}{A(\boldsymbol{\omega})} \right|^2. \end{aligned} \quad (1.20)$$

The noise term considered to obtain Eq. (1.20) is a zero-mean sequence with power spectrum:

$$S_E(\boldsymbol{\omega}) = |A(\boldsymbol{\omega})B(\boldsymbol{\omega})|^2, \quad (1.21)$$

where $A(\boldsymbol{\omega})$ and $B(\boldsymbol{\omega})$ are two polynomial terms of the AR and MA coefficients of the model. In the

derivation of Eq. (1.20), an algorithm is found for computing the AR and MA coefficients. We start from the definition of power spectrum for a stochastic process, which is the squared amplitude of the Fourier transform of its autocorrelation function r . Multiplying every term in Eq. (1.19) by $i(\mathbf{x} - \mathbf{t})$ and computing its expected value, we obtain

$$\begin{aligned} E[i(\mathbf{x})i(\mathbf{x} - \mathbf{t})] &= E \left[\sum_{\mathbf{r} \in R} \theta_{AR}(\mathbf{r})i(\mathbf{x} - \mathbf{r})i(\mathbf{x} - \mathbf{t}) \right] \\ &\quad + E \left[\sqrt{v}\varepsilon(\mathbf{x})i(\mathbf{x} - \mathbf{t}) \right]. \end{aligned} \quad (1.22)$$

This can be rewritten in terms of the correlation function as

$$r_I(\mathbf{t}) = \sum_{\mathbf{r} \in R} \theta_{AR}(\mathbf{r})r_I(\mathbf{t} - \mathbf{r}) + \sqrt{v}r_{EI}(\mathbf{t}). \quad (1.23)$$

Repeating the same operation but multiplying by $\varepsilon(\mathbf{x} - \mathbf{t})$

$$r_{EI}(\mathbf{t}) = \sum_{\mathbf{r} \in R} \theta_{AR}(\mathbf{r})r_{EI}(\mathbf{t} - \mathbf{r}) + \sqrt{v}r_E(\mathbf{t}). \quad (1.24)$$

Fourier transforming Eqs. (1.23) and (1.24) and combining them with Eq. (1.21), an expression for the autocorrelation function is found:

$$\begin{aligned} R_I(\boldsymbol{\omega}) &= \frac{\sqrt{v}}{A(\boldsymbol{\omega})} R_{EI}(\boldsymbol{\omega}) \\ &= \frac{v}{A(\boldsymbol{\omega})^2} R_E(\boldsymbol{\omega}) \\ &= \frac{v}{A(\boldsymbol{\omega})^2} A(\boldsymbol{\omega})B(\boldsymbol{\omega}) \\ &= \frac{vB(\boldsymbol{\omega})}{A(\boldsymbol{\omega})}. \end{aligned} \quad (1.25)$$

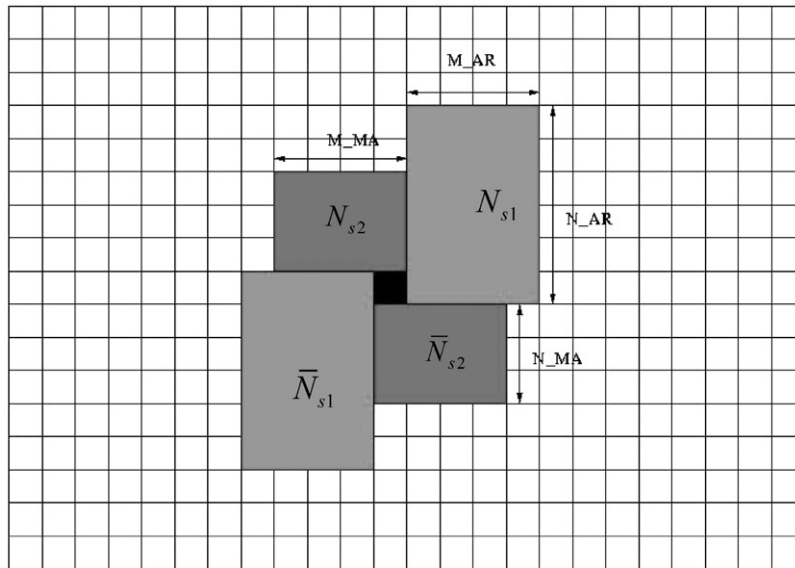


Fig. 2. Support regions for the ARMA models. N_AR and M_AR determine the size of the AR support region and N_MA , M_MA , the size of the MA support region. N_1 and N_3 are composed of N_{s1} and \bar{N}_{s1} . N_2 is composed of N_{s2} and \bar{N}_{s2} .

From Eq. (1.25), the expression for power spectrum (1.20) can be directly obtained. Unlike the 1-D case, the driving noise ε cannot be replaced by a finite moving average representation excited by an independent identically distributed sequence, as in AR, since $\sqrt{A(\omega)B(\omega)}$ is not, in general, a finite-order polynomial. Also note that AR models can be included as a special case of ARMA models in which $B(\omega) = 1$.

ARMA models, like AR models, can be causal, semi-causal and non-causal. In this work, a non-causal ARMA model is used leading to a reduction in the order of the model.

The parameters of the ARMA model can be estimated by two methods [12], one based on correlations, and the other based on maximum likelihood. Here the correlation method is chosen because its computational demand is smaller, and its results are accurate enough when the order of the ARMA model is small compared with the image size. The models considered so far had 7320 parameters and the image sizes were $512 \times 512 = 262,144$, or $1024 \times 1024 = 1,048,576$; so the above condition was met.

The method considers three subsets of $\{\mathbf{Z}^2 - (0,0)\}$, N_1 (the support region for the AR

part of the model), N_2 (the support region for the MA part of the model) and N_3 (a set of neighbors to obtain the AR coefficients). Each N_i is a finite symmetric set composed of anti-symmetric subsets N_{si} and \bar{N}_{si} defined by

$$N_i = N_{si} \cup \bar{N}_{si},$$

$$N_{si} \cap \bar{N}_{si} = 0,$$

$$(i,j) \in N_{sk} \Rightarrow (-i,-j) \notin N_{sk}.$$

The subsets used in this work are shown in Fig. 2. The symmetry of the correlation function $r(\mathbf{r}) = r(-\mathbf{r})$, implies that the coefficients of the model are symmetric $\theta_{AR}(\mathbf{r}) = \theta_{AR}(-\mathbf{r})$, $\theta_{MA}(\mathbf{r}) = \theta_{MA}(-\mathbf{r})$ and Eq. (1.19) can be rewritten as

$$i(\mathbf{x}) = \sum_{\mathbf{r} \in N_{s1}} \theta_{AR}(\mathbf{r})(i(\mathbf{x} - \mathbf{r}) + i(\mathbf{x} + \mathbf{r})) + \sqrt{v}\varepsilon(\mathbf{x}), \quad (1.26)$$

where the cross-correlation between the image and the noise ε is

$$r_{EI}(\mathbf{r}) = E[\varepsilon(\mathbf{x})i(\mathbf{x} + \mathbf{r})] = \begin{cases} \sqrt{v} & \text{if } \mathbf{r} = \mathbf{0}, \\ \sqrt{v}\theta_{MA} & \text{if } \mathbf{r} \in N_2, \\ 0 & \text{otherwise.} \end{cases} \quad (1.27)$$

With Eqs. (1.26) and (1.27), it is possible to derive the calculation procedure. Multiplying by $y(\mathbf{0})$, $y(\mathbf{x} + \mathbf{s})$, $\mathbf{s} \in N_{s2}$, $y(\mathbf{x} + \mathbf{t})$, $\mathbf{t} \in N_{s3}$ and taking expectation we obtain, respectively:

$$r(\mathbf{0}) = 2 \sum_{\mathbf{r} \in N_{s1}} \theta_{AR}(\mathbf{r})r(\mathbf{r}) + v, \quad (1.28)$$

$$r(\mathbf{s}) = \sum_{\mathbf{r} \in N_{s1}} \theta_{AR}(\mathbf{r})(r(\mathbf{s} - \mathbf{r}) + r(\mathbf{s} + \mathbf{r})) + \sqrt{v}\theta_{MA}(\mathbf{s}), \quad \mathbf{s} \in N_{s2}, \quad (1.29)$$

$$r(\mathbf{t}) = \sum_{\mathbf{r} \in N_{s1}} \theta_{AR}(\mathbf{r})(r(\mathbf{t} - \mathbf{r}) + r(\mathbf{t} + \mathbf{r})) \quad \mathbf{t} \in N_{s3}. \quad (1.30)$$

The following algorithm is applied:

1. Choose the sets N_1 , N_2 and N_3 . N_3 must be the symmetric set having the n nearest points to the origin so that $N_2 \cap N_3 = \mathbf{0}$, where n is the size of N_{s1} . The condition of no intersection between N_2 and N_3 is required because if some particular \mathbf{s} belongs at the same time to N_2 and N_3 , this will lead to a corresponding MA coefficient of value zero (this can be easily verified from Eqs. (1.29) and (1.30)). Nevertheless, note that N_3 is not unique. The sets selected in this work are represented in Fig. 2. N_3 is chosen to be the same as N_1 .
2. Estimate the various correlation terms needed:

$$\hat{r}(\mathbf{r}) = \frac{1}{N} \sum_{\mathbf{x}} i(\mathbf{x})i(\mathbf{x} + \mathbf{r}), \quad (1.31)$$

where N is the number of pixels where the two shifted versions of the image overlap. In our programs, this is done efficiently using FFTs.

3. Solve the linear system in Eq. (1.30), using the correlation estimates from the preceding step to obtain the AR coefficients of the model. It is worth noting that the system is close to singularity; so usual techniques for linear system solving do not apply. We have used the singular value decomposition algorithm [13], which allows specifying a tolerance for the eigenvalues of the system matrix, eliminating those that are too small.
4. Solve the equation in Eq. (1.28), replacing each θ_{AR} by its estimate, and obtain the term v .
5. Solve each equation in Eq. (1.29) for the corresponding MA coefficient, replacing the

estimated values for θ_{AR} and v obtained in steps 3 and 4.

6. Finally, the power spectrum is determined using the variant given for a toroidal ARMA model [12], since it has been found to be more accurate for our images:

$$S_I^{ARMA}(\boldsymbol{\omega}) = \left| \sqrt{v \frac{1 + \sum_{\mathbf{r} \in R} \theta_{MA}(\mathbf{r})e^{-2\pi i(\boldsymbol{\omega} \cdot \mathbf{r})}}{1 - \sum_{\mathbf{r} \in R} \theta_{AR}(\mathbf{r})e^{-2\pi i(\boldsymbol{\omega} \cdot \mathbf{r})}}} \right|^2 = \left| \sqrt{v \frac{B(\boldsymbol{\omega})}{A(\boldsymbol{\omega})}} \right|^2. \quad (1.32)$$

For our purposes, it is additionally supposed that we are processing images where the signal comes mainly from the noise terms of Eq. (1.14) (thus the specimen spectrum is negligible), and that the noise before image formation is white. Under these assumptions, the spectrum $S_I^{ARMA}(\boldsymbol{\omega})$ is an estimation of the squared modulus of the CTF plus the background term of noise after image formation:

$$S_I^{ARMA}(\boldsymbol{\omega}) \simeq S_I(\boldsymbol{\omega}) = |H(\boldsymbol{\omega})|^2 + S_{N_a}(\boldsymbol{\omega}). \quad (1.33)$$

4. Parameter adjustment algorithm

The estimation of the power spectrum produces an image of the same size as the original with the values of the power spectrum for every pixel. To adequately estimate the parametric expression of the CTF, we need to extract the values of the CTF physical parameters from Eq. (1.33). This is done by adjusting the CTF model in question to the power spectrum obtained by the ARMA modeling. The process performs a 2-D surface adjustment over the 24 parameters of the theoretical model. No rotational averaging is done in any way, so that the presence of astigmatism can be detected and images affected by it can be adequately treated.

Based on the spectra observed in our images, and on previous models [7], we have found that exponential functions fit the background noise term fairly well. We propose a function of three

terms to reproduce the observed behavior:

$$\begin{aligned}
 S_{N_a}(\omega) &= b + K_g \exp \left[-\frac{(\omega_U - \omega_{U0})^2}{2s_{gU}^2} - \frac{(\omega_V - \omega_{V0})^2}{2s_{gV}^2} \right] \\
 &\quad + K_s \exp \left[-\frac{\sqrt{|\omega_U|}}{s_{sU}} - \frac{\sqrt{|\omega_V|}}{s_{sV}} \right], \\
 \omega_U &= \omega_X \cos(\theta_a) + \omega_Y \sin(\theta_a), \\
 \omega_V &= -\omega_X \sin(\theta_a) + \omega_Y \cos(\theta_a). \tag{1.34}
 \end{aligned}$$

The first constant term b is intended to adjust the high spatial frequency base level of the spectrum, the second term is a gaussian function to adjust medium spatial frequencies, and the third term reproduces the shape of the spectrum at low spatial frequencies quite well. The angle θ_a allows for considering an anisotropic noise spectrum, and ω_{U0} , ω_{V0} are values to shift the gaussian from the center of coordinates so that the middle spatial frequency range can be better adjusted. It must be pointed out that the anisotropic noise considered here is not directly due to the microscope, but can be the result of the composition of different effects subsequent to image formation, such as the effect of the scanner on the digitalization step of the micrograph. The noise model amounts to a total of 10 parameters: b , K_g , s_{gU} , s_{gV} , ω_{U0} , ω_{V0} , K_s , s_{sU} , s_{sV} , θ_a . The 2-D nature of the search performed forces us to duplicate s_g , s_s and ω_0 , and introduce the angle θ_a . The background noise, ideally, would have to coincide with the power spectrum surface in all the CTF zeros (which are the minima of the surface) and in high spatial frequencies where the CTF is attenuated. In one dimension, the model has 6 parameters, differing from previous models [7] only in the constant term b and the displacement term ω_0 . In fact, if the images used are not astigmatic, the values that our programs are able to find look very similar in both directions, and the model can eventually be reduced to working in one dimension to cover this situation.

We discovered in the course of our experiments that a good adjustment of this background term is crucial for a satisfactory final adjustment and parameter estimation. We therefore developed a stepwise search algorithm that basically finds first

the best background term and then adjusts the parametric CTF shown in Eq. (1.6). This procedure is described in the next section.

5. Search method

Due to the considerations made in the description of the CTF model, some of the least relevant parameters for the CTF shape are masked because of their relatively small influence at medium resolution. This implies that a large number of local minima exist in the search space, complicating an accurate determination of these CTF parameters. For this reason, our program performs a gradual approach to the solution that guarantees that the CTF function is fitted and the parameters have physical meaning, although some variation in the less sensitive parameters may occur when treating medium resolution images.

The optimization method used is Powell's algorithm [13], an efficient algorithm for minimization of a multidimensional function when no explicit function is available for the gradient, although it is sub-optimal in the sense that it can be trapped in a local minimum. Therefore this algorithm is run not once, but many times in a sequence of steps consisting of (i) determination of the background noise, (ii) determination of the physical CTF model, (iii) weighted optimization and (iv) fine tuning of the model.

The background noise determination starts with the calculation of b . It is computed as the average of the power spectrum values for high spatial frequencies. Then the term dependent on the square root of the spatial frequency is computed in three phases: (a) least-squares adjustment to obtain an initial solution, (b) optimization of the L1 norm of the error to fit better the zones of the curve that have lower values, and (c) gradual penalization of this term so that it is always under the power spectrum. This objective is achieved by heavily penalizing the L1 fitting error in those cases where the fitting surface is above the spectrum. Extreme changes in the penalization factor value tend to make the algorithm unstable, and therefore a strategy of gradually increasing penalizations is used, starting with a value of 2 and

increasing it in powers of 2 up to the value given by the user. In our experiments, this value is 128. Finally, the gaussian term is found, first by varying only the parameters $K_g, s_{gU}, s_{gV}, \omega_{U0}, \omega_{V0}$ in a least-squares fit and then globally optimizing all the ten parameters for the background noise.

It is important to note that we have used the L1 norm of errors in the distance calculations of the optimizing algorithm, and not the L2 norm, since the latter tends to give more importance to large errors, and we are interested in fitting the small details present mostly in the CTF and not in the noise. The L2 norm has been implicitly used only during the least-squares first step of the parameter search, precisely where large errors occur.

Once the background noise is adjusted, an exhaustive search over the defocus in the X - and Y -axis is done, supposing that the astigmatism is not rotated, i.e. that the angle θ in Eq. (1.4) is zero. For each defocus combination, the α semi-angle and K of Eqs. (1.9) and (1.6) are estimated by a simple least-squares method. Next, all the parameters of the CTF model in Eq. (1.6) are found, minimizing the weighted relative error with Powell’s algorithm. This distance function of the weighted relative error is used here and in subsequent steps because of the need to concentrate the search on the values of the CTF lobes, which are usually very small compared with that of the noise. Following the gradual relaxation of the imposed restrictions, a global optimization is done, allowing the variation of all 24 parameters, but still penalizing the background noise.

A good approximation of the power spectrum has now been obtained, but two drawbacks remain to be overcome. First, the parametric CTF model has values much lower than those of the noise, and even in the case of good numeric approximation, the shape of the CTF could not have been adequately modeled. Secondly, the penalization imposed on the noise term keeps it well under the curve, holding down with it the parametric CTF described by Eq. (1.6). The solution adopted in this algorithm is to increase progressively the parametric CTF weight

in the distance function according to the spatial frequency modulus ω :

$$W_x(\omega) = \begin{cases} \frac{1}{x} - 1 + e^{\ln(2-1/x)(\omega-\omega_{\min})/(\omega_1-\omega_{\min})}, & \omega_{\min} < \omega < \omega_1, \\ 1, & \omega_1 < \omega < \omega_3, \\ e^{-\ln(1/x)(\omega-\omega_3)/(\omega_{\max}-\omega_3)}, & \omega_3 < \omega < \omega_{\max}, \\ 0, & \text{otherwise.} \end{cases} \tag{1.35}$$

The spatial frequencies ω_{\min} and ω_{\max} represent 10% and 90% of the maximum signal-related spatial frequency present in the micrograph; ω_1 and ω_3 are the spatial frequencies of the first and third zeros, respectively, and x is the weighting parameter, ranging from 2 to 1024 in powers of two. Once the CTF has been given more importance, the weight of the background term is gradually reduced and a new optimization is run.

So far, to increase the speed of the distance function evaluation, the power spectrum values were taken every 8 pixels. Although good results are obtained, a final tuning step is done, this time optimizing all the parameters, without background noise penalization and evaluating over all the pixels. Only the weighting strategy to enhance the fit between the first and third zeros is maintained.

As can be seen in Fig. 3, very good approximations fulfilling our objective of adequately modeling the CTF have been achieved.

6. Interpolation of CTF functions

In practice, every point of a micrograph is affected by a different CTF function. Ideally, it would be desirable to know this function in all cases, but this is not actually feasible. In this work, the micrograph is divided into small sections of varying size and the CTF is computed for each one of these regions following the ARMA and the parametric CTF adjustment explained so far. Here 512×512 pixel sections have been used. Although the ARMA model of smaller

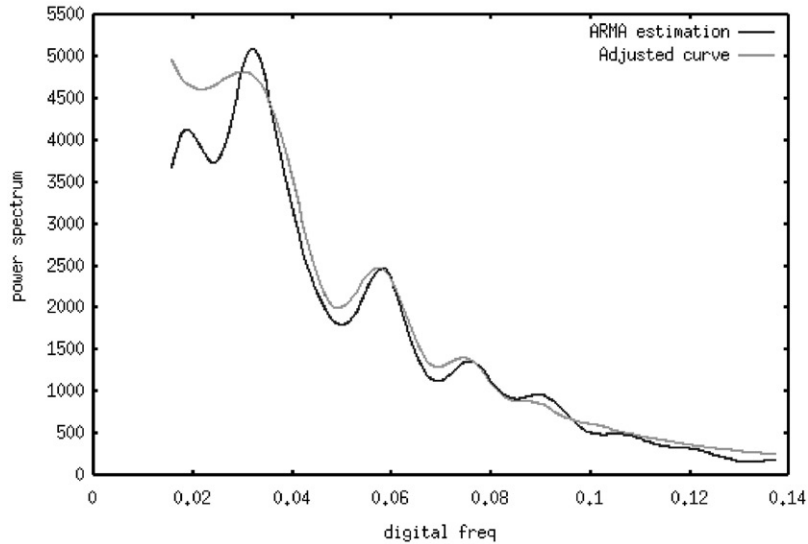


Fig. 3. Profile along a line through the x -axis of an ARMA estimation and its adjusted curve using the search algorithm outlined in the text. The first three zeros of the CTF seem to have been adequately detected, and a good approximation of the amplitudes achieved. The original data came from a 512×512 pixels section of a carbon-coated grid cryomicrograph taken with a FEG microscope at 200 kV. The sampling rate is $3.27 \text{ \AA}/\text{pixel}$. Spatial frequencies lower than 10% of the maximum present in the micrograph and greater than 90% have not been represented as they were not included in the adjustment.

regions can be calculated, this size is a good balance between the increased accuracy observed when larger regions are modeled, and the higher number of local CTFs that must be calculated with smaller regions. Next, the power spectrum is adjusted to each selected particle, using the following interpolation scheme: (1) Calculate the distance and relative position of the central point of the particle image to the central point of the nearest four regions where an ARMA model has been estimated. If the particle is on the border of the micrograph, only the two nearest regions are used to interpolate, and if it is in a corner, the power spectrum of the corner's region is assigned to the particle without interpolation. (2) Next, weights are assigned to the regions based on the previously computed distances, and (3) a bilinear interpolation is performed to obtain the particle's associated power spectrum function. This interpolation is an approximation that could be avoided if an ARMA model is performed over the particle region, at the cost of increasing the computational time when a

large number of particles is present in the micrograph.

7. Results

We have tested our programs with simulated and experimental data coming from studies of negative staining microscopy as well as cryomicroscopy, using carbon-coated and non-carbon-coated grids.

To start with, a quantitative comparison test between the ARMA models and the periodogram was done using simulated data. A CTF of given parameters (see Table 1) was applied to a total of 1470 noisy images whose pixel density was distributed as $N(0,1)$, and their periodogram averaging and ARMA models were calculated over the images. The conditions used for this experiment included two sizes (512, 1024 pixels), five defocus values (4000, 8000, 12,000, 16,000, 24,000 \AA), and seven AR and MA orders (16, 20, 24, 26, 30, 34, 38), in all their possible combinations. Three

realizations of every set of values were performed and their error figures, averaged for the ARMA models, as well as for the periodogram averaging,

Table 1

Images containing white noise were generated and a given CTF was then applied

| Parameter | Value |
|---|---|
| K | 1.3 |
| Sampling rate | 3.5 Å/pixel |
| Voltage, V | 100 kV |
| DefocusU Δf_U , DefocusV Δf_V | Variable, 4000, 8000, 12,000, 16,000 and 24,000 Å |
| Spherical aberration, C_s | 5.5 mm |
| Chromatic aberration, C_a | 6 mm |
| Energy loss $\Delta U/V$ | 9.8 ppm = 9.8×10^{-6} V/V |
| Longitudinal displace, ΔR | 79 Å |
| Convergence cone, semi-angle, α | 0.2 mrad |
| Gaussian K , K_g | 1.8 |
| SigmaU s_{gU} , SigmaV s_{gV} | 160 |
| Sqrt.K, K_s | 40 |
| SqU s_{sU} , SqV s_{sV} | 17 |
| Base line, b | 0.2 |

The CTF parameters used in the simulation are shown in this table. Those parameters not present in this table are supposed to be zero. Their values were based on previous work on cryomicroscopy data.

were computed. The parameters applied for the periodogram averaging were the optimal ones determined in [11] by Fernández et al.

To measure the fitness of these models we generated an image with the simulated CTF value at every pixel, called the CTF-image from here on. Then the ARMA model (ARMA-image) and the periodogram averaging of the image (PA-image) were calculated. The L1 norm of the error between the CTF-image and the ARMA-image was computed over those pixels ranging in spatial frequencies between the first and third zeros of the CTF. Then, the Fourier transform of the CTF-image and ARMA-image were calculated, and their amplitudes were compared, again with an L1 norm. Finally, a weight of 50% was applied to every measure as in the following expression:

$$\begin{aligned} \text{Error} &= \frac{1}{2} \frac{L1_{\text{zeros}} - \min[L1_{\text{zeros}}]}{\max[L1_{\text{zeros}}] - \min[L1_{\text{zeros}}]} \\ &+ \frac{1}{2} \frac{L1_{\text{fit}} - \min[L1_{\text{fit}}]}{\max[L1_{\text{fit}}] - \min[L1_{\text{fit}}]} \end{aligned} \tag{1.36}$$

The combined use of the real and Fourier space measures allows the estimation of the error

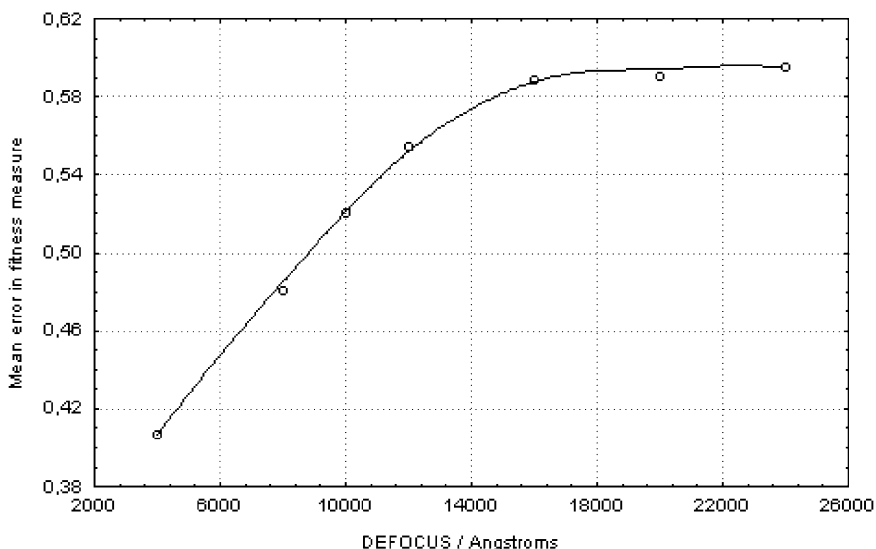


Fig. 4. Variation of the error figure against the defocus in the simulated ARMA models. Every point is an average over those models with a given defocus.

committed in determining the CTF values in the region of interest (between the first and the third zeros) as well as in its shape (better captured in Fourier space). The use of the L1 norm of the error is intended to avoid giving more importance to larger errors.

The results obtained from the comparison of the ARMA models with the periodogram averaging

using the error figure in Eq. (1.36) were conclusive. For the simulated data with variable defocus and image size, the ARMA estimation was better in all the 1470 cases, independently of the ARMA order used. This can also be said for experimental data, at least visually, as will be shown below.

Some dependence of the optimal ARMA order on the image size and defocus can be expected a

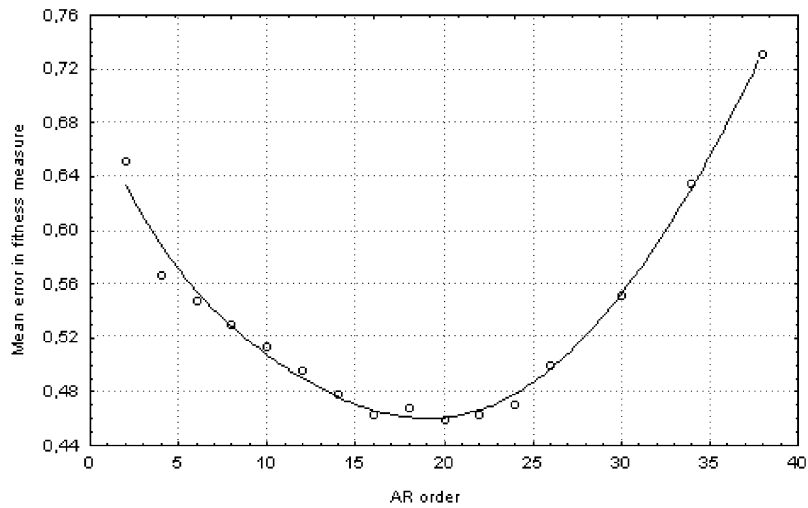


Fig. 5. Variation of the error figure against the AR order in the simulated ARMA models. Every point is an average over those models with a given AR order.

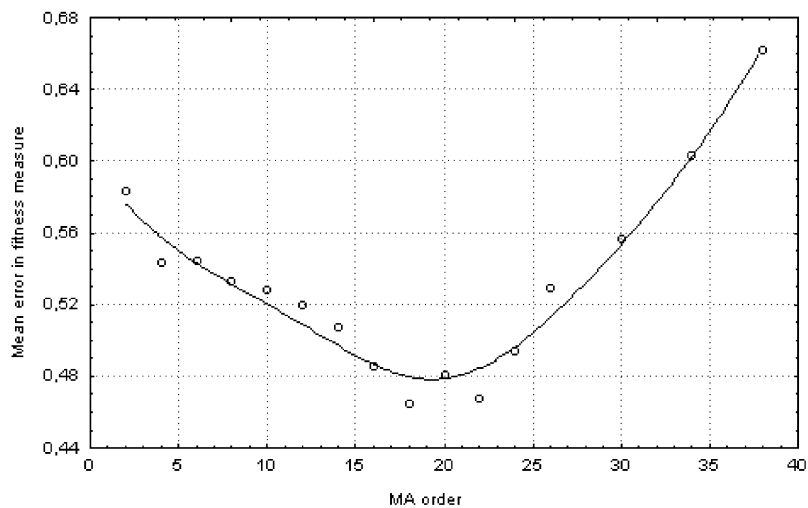


Fig. 6. Variation of the error figure against the MA order in the simulated ARMA models. Every point is an average over those models with a given MA order.

Table 2
Optimal ARMA orders for the simulated CTF data in all the conditions tested

| Size (pixels) | Defocus (Å) | Optimal AR order | Optimal MA order | Error figure |
|---------------|-------------|------------------|------------------|--------------|
| 512 | 4000 | 26 | 16 | 0.30588 |
| 512 | 8000 | 20 | 26 | 0.37700 |
| 512 | 10,000 | 22 | 20 | 0.40334 |
| 512 | 12,000 | 20 | 16 | 0.44568 |
| 512 | 16,000 | 24 | 16 | 0.45339 |
| 512 | 20,000 | 20 | 20 | 0.48016 |
| 512 | 24,000 | 20 | 16 | 0.48961 |
| 1024 | 4000 | 26 | 30 | 0.10050 |
| 1024 | 8000 | 24 | 30 | 0.17554 |
| 1024 | 10,000 | 24 | 18 | 0.21140 |
| 1024 | 12,000 | 26 | 16 | 0.23284 |
| 1024 | 16,000 | 26 | 16 | 0.24696 |
| 1024 | 20,000 | 22 | 16 | 0.24792 |
| 1024 | 24,000 | 24 | 16 | 0.23644 |

The rest of the CTF parameters were those of [Table 1](#). The order AR 24, MA 20, was not significantly different from the best order in all the cases.

priori. The image size can limit the maximum ARMA order while the rapid oscillations caused by a high defocus may demand higher model orders. To elucidate this point, we explored the error figure for all the models in the previous experiment, plus an added set of models of order AR and MA 2, 4, 6, 8, 10, 12, 14, in all possible combinations, again varying the defocus and size of the simulated images.

An analysis of the results shows that the error of the ARMA models tends to decrease with the increase in size: an average value of the error was 0.54 for the 512 × 512 images whereas 0.23 for the 1024 × 1024 images. As far as dependence on the defocus is concerned, [Fig. 4](#) shows that when the defocus is higher, and consequently the CTF curve has more oscillations, the error increases until it reaches a plateau. More interestingly, the error figure for the AR and MA orders of the ARMA model, averaged over all the conditions

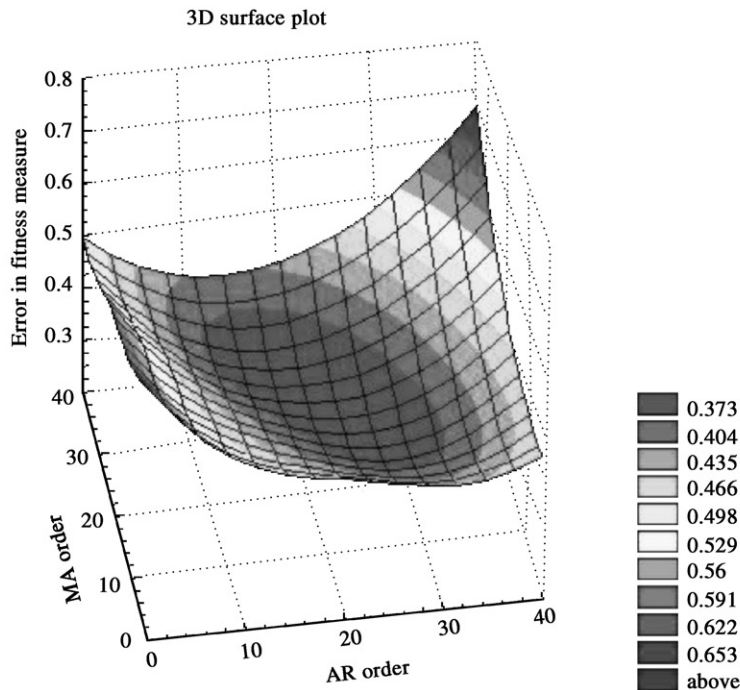


Fig. 7. 3-D graph showing the error figure in ARMA models. It can be seen that there is a region, around 15–25 in AR and 20–30 in MA orders, where the ARMA models have minimum error.

used, shows that there is an optimal value for them, near 20 (see Figs. 5 and 6). For the AR models used in previous works [11], it was found that better results were obtained by increasing the AR order (up to 60), but here the presence of a minimum in a relatively low AR order value implies a reduction in the number of coefficients used, thus stabilizing the model and requiring less computation time. This is not accomplished at the cost of reduced accuracy, since the error figure shows that the best ARMA models are superior to the best of our previous AR models [11] (data not shown).

A more detailed study of the estimation error of the ARMA models as a function of the AR and MA order, image size and specific image simulation parameters shows that the optimal value of the AR and MA order was different for every

experimental condition simulated (Table 2). However, it was also found that the combination of AR order 24 and MA order 20 was always present in the best choices for all conditions tested (Fig. 7). Therefore, these were the order values used in our tests with experimental data.

The tests with experimental micrographs were done with data obtained from different techniques and microscopes. Negative staining microscopy micrographs came from a Jeol 1200 Ex-II, 100 kV microscope. Carbon-coated grids cryo-micrographs came from a Phillips CM120 operating at 100 kV, and finally non-carbon-coated grids cryo-micrographs were taken with a Philips CM200FEG operated at 120 kV. The results appear in Figs. 8–10, showing that the ARMA models give a clearer determination of the CTF rings. The results for non-carbon-coated grids cryo-micrographs are

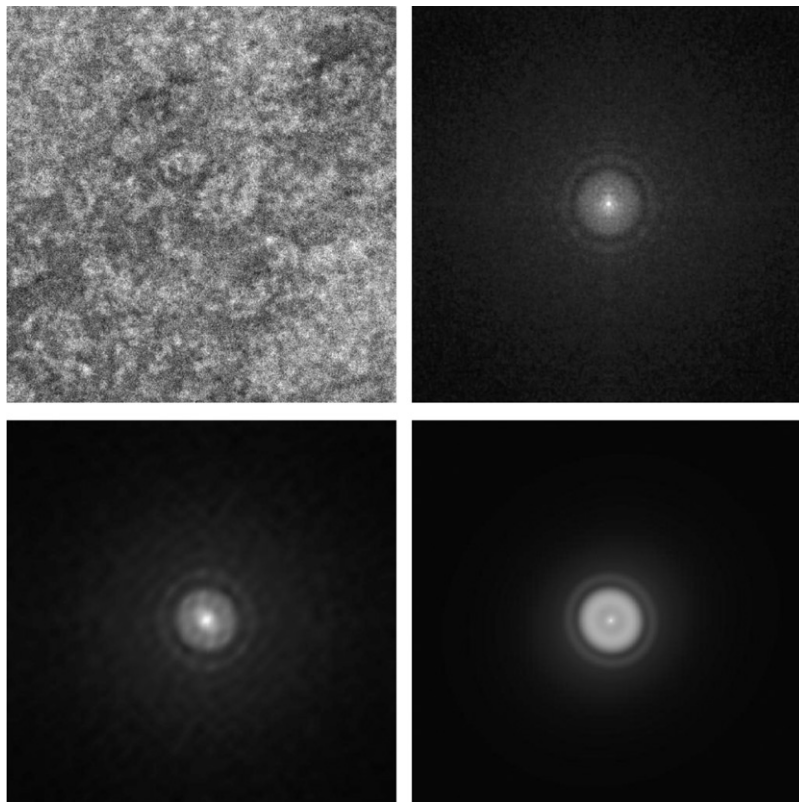


Fig. 8. Results of CTF estimation for negative stain micrographs. Upper left: original data (512×512 pixels). Upper right: periodogram-averaging estimation of the CTF (sections of 64×64 pixels, 32 pixels of overlapping in both directions and padding up to 512 pixels). Lower left: ARMA estimation of order 24, 20. Lower right: model CTF function generated with the estimated parameters.

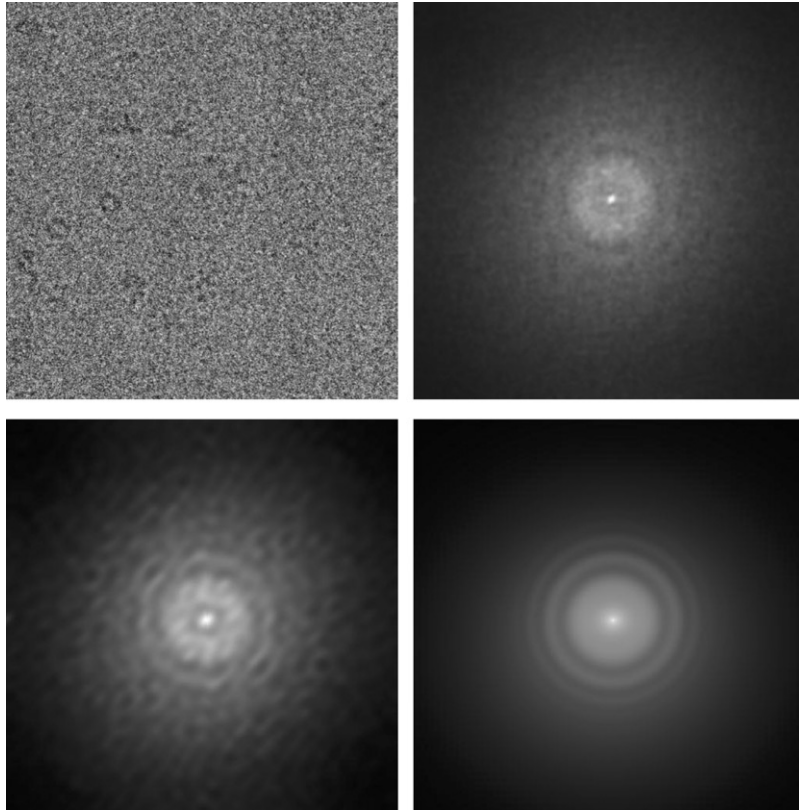


Fig. 9. Results of CTF estimation for carbon-coated holey grid cryo-micrographs. Upper left: original data. Upper right: periodogram averaging. Lower left: ARMA estimation. Lower right: Model. See Fig. 8 for details.

especially interesting (Fig. 10), since it is difficult to detect the CTF in such conditions by classical methods [14]. Fig. 11 shows a profile and the radial average of the corresponding ARMA and PA-images for the non-carbon-coated grids micrograph showing the superiority of the ARMA-based estimation over periodogram averaging.

Finally, the possibility of performing ARMA averaging over different regions of a micrograph was considered. This methodology would be of interest when dealing with extremely faint CTFs. An experiment with simulated data was carried out: 100 individual ARMA models were computed for small regions of a micrograph with constant defocus (10,000 Å). Their error figure turned out to be 0.42868 ± 0.0196 . If the set of 100 models is divided into 10 groups with 10 models each and an average performed within each group, then

the error of the average estimation per group decreases to 0.34868 ± 0.0132 . The two values were found to be statistically different at 95% confidence by Student's test. These results suggest that averaging could be an acceptable practice with ARMA models.

8. Discussion

The studies presented in this work on the applicability of ARMA models to CTF estimation of electron micrographs have shown that this approach is indeed valuable, although as with all methods, a thorough understanding of how they should be applied is essential.

The experiments that were carried out show that the order of the ARMA model depends on the

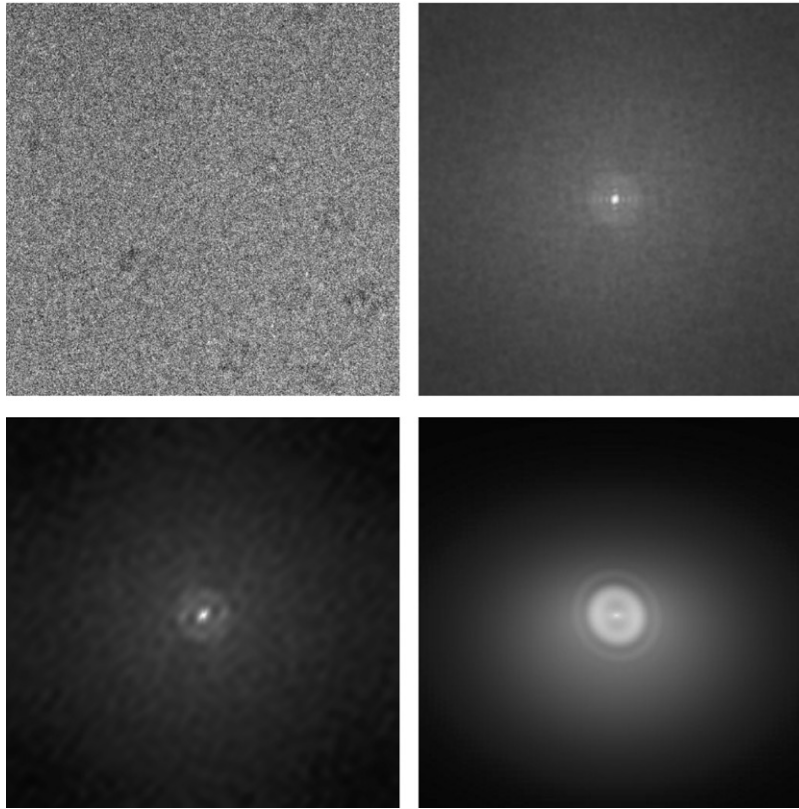


Fig. 10. Results of CTF estimation for non-carbon-coated holey grid cryo-micrographs. Upper left: original data. Upper right: periodogram averaging. Lower left: ARMA estimation. Lower right: Model. See Fig. 8 for details.

image size and the defocus of the micrograph. However, the good news is that there exists a set of ARMA models statistically indistinguishable from the optimal order for each size and defocus combination. Thus, in a practical application, the AR order can range from 20 to 30, and the MA order from 15 to 25. It has also been shown that with increased image size, keeping the ARMA order constant, reduces the estimation error. This could be explained by the fact that more data for calculating autocorrelation values are available.

Fig. 7 shows that a combined use of the AR part and the MA part on ARMA models improves on the results of purely AR or MA ones. The AR model is responsible for the main part of the CTF shape fitting while the MA coefficients are very helpful in the fine adjustment of the CTF values. This is the reason why our ARMA

orders are much lower than those previously determined [11].

It should be pointed out that high-order pure AR models usually produce spikes in the spectrum [11]. However, the 2-D error function used effectively in this work favors the selection of less spiky estimations.

A typical running time for performing an ARMA estimation of order 24, 20 on a 512×512 section of a micrograph is 1–2 min in our computers (an SGI Origin 200 SGI with R12000 processors at 360 MHz. This time can reach up to 4–5 min in a Pentium III at 800 MHz, running under Linux.) The algorithm complexity is $O(n(\text{AR}^2 + \text{MA}^2))$ where n denotes the total number of pixels, and AR and MA the orders of the model selected. The program has been used with micrographs as big as 3000×3000 and as

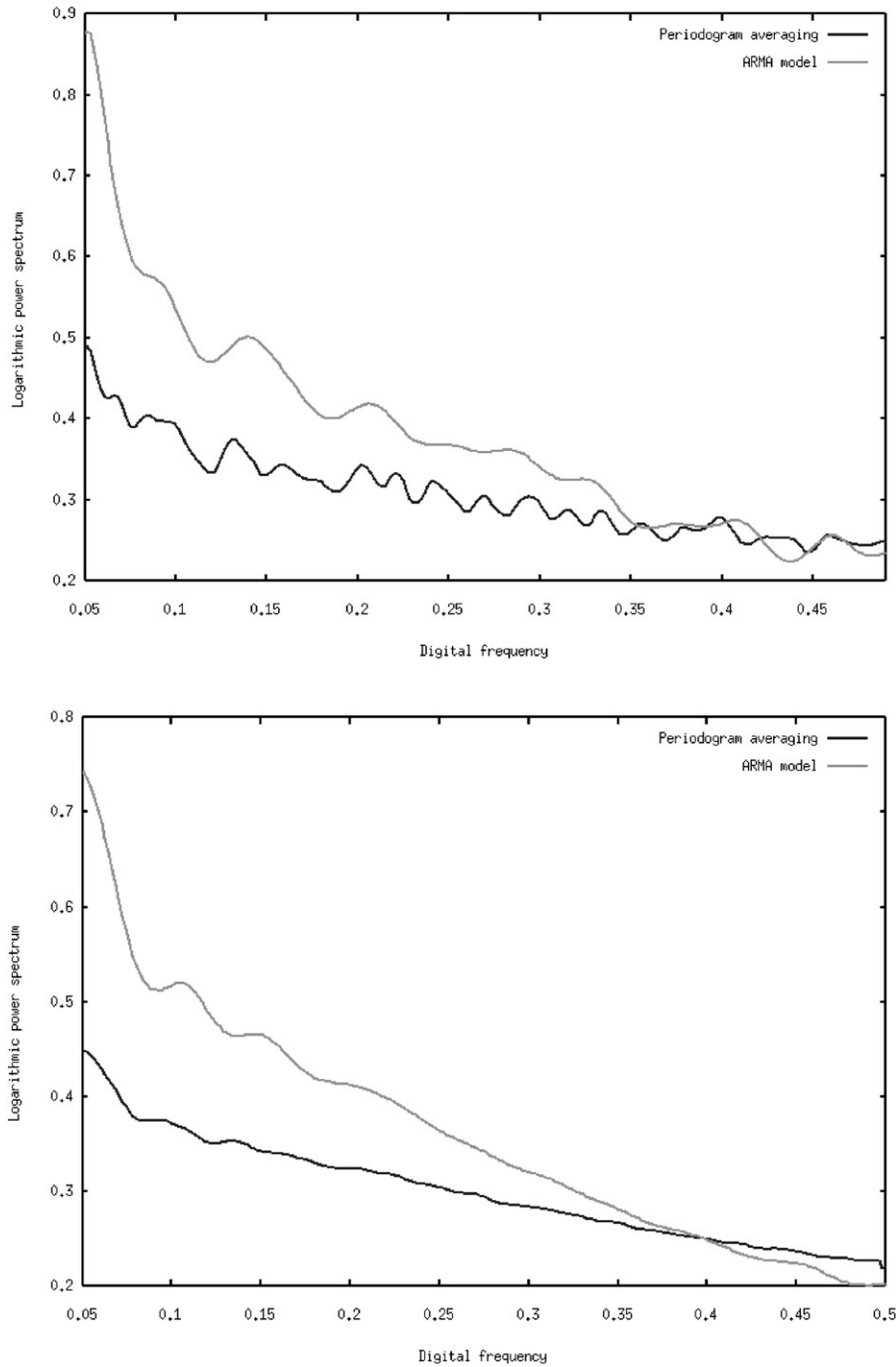


Fig. 11. Upper graph: profile along the zero spatial frequency axis in x -direction of the CTF estimations. It is clearly seen that ARMA estimation is a technique that reveals its usefulness in the most difficult experimental conditions, where the periodogram averaging offers poor results. Left: radial averages of the CTF estimations. ARMA allows a clearer detection of the first three zeroes of the CTF than the periodogram averaging. Data are the same as that for Fig. 10. Digital spatial frequencies lower than 0.05 are not shown, as they would not be used in the adjustment of the CTF model.

small as 200×200 pixels without problems. However, it should be pointed out that in the latter case, we are near the practical limits of applicability of our algorithmic implementation of ARMA.

The theoretical CTF fitting algorithm has a typical running time of 10 min in the same situation cited above, its complexity being roughly $O(nk)$ where k is the number of parameters to estimate. However, this time is highly variable, depending on the accuracy of the first estimation provided by the user, as well as the subsampling rate applied to the ARMA-image at the first stages of the search.

In the course of our experiments, we found that the ARMA algorithm may become unstable if applied to low pass filtered images. This was detected by the appearance of anomalous peak regions in the ARMA image. This is due to the presence of spatial frequencies with zero value in the power spectrum, which cannot be properly treated by the AR part of the model. For this reason, the use of the approach with hard-filtered images should be avoided. Normalizing the image values before applying ARMA modeling is also recommended for avoiding numerical instabilities.

9. Conclusions

In this work, a new technique for the practical estimation of the CTF on electron micrographs has been introduced and compared with those currently in use. It has been shown that much better estimations can be obtained by means of parametric ARMA modeling with a truly 2-D consideration of the estimation problem, thus allowing the treatment of difficult scenarios like the effects of astigmatism and the low contrast when ice is used as the only support of the specimen sample. The ARMA technique also adds stability and takes less computing time than formerly used AR models, there being fewer parameters to calculate.

A theoretical CTF model with a full description of the underlying physics is adjusted to the ARMA spectral estimation. The fitting algorithm works

with a high number of parameters although the theoretical model can be reduced to a simpler one without losing accuracy, except for very high-resolution studies.

An interpolation scheme has been implemented to produce a CTF estimation for every particle projection involved in the image processing. All programs developed for the task are fully available and free as part of the Xmipp software package for 3D electron microscopy at www.biocomp.cnb.uam.es.

Acknowledgements

Partial support is acknowledged from the “Comisión Interministerial de Ciencia y Tecnología” of Spain through projects BIO98-0761, BIO2001-1237, TIC99-0361 and TIC2002-00228, and from the NIH through grant 1R01-HL70472. The authors wish to thank our colleagues in the laboratory Yolanda Robledo and Montserrat Bárcena, as well as Alok Mitra from the School of Biological Sciences, University of Auckland, who kindly supplied us with the electron micrographs.

References

- [1] H.P. Erickson, A. Klug, *Phil. Trans. R. Soc. London B* 261 (1971) 105.
- [2] J. Frank, *Optik* 38 (1973) 519.
- [3] J. Frank, *Three Dimensional Electron Microscopy of Macromolecular Assemblies*, Academic Press, San Diego, 1996.
- [4] K.J. Hanszen, *The optical transfer theory of the electron microscope: fundamental principles and applications*, in: *Advances in Optical and Electron Microscopy*, Vol. 4, Academic Press, New York, 1971, pp. 1–84.
- [5] Z.H. Zhou, S. Hardt, B. Wang, M.B. Sherman, J. Jakana, W. Chiu, *J. Struct. Biol.* 116 (1) (1996) 216.
- [6] S.J. Ludtke, P.R. Baldwin, W. Chiu, *J. Struct. Biol.* 128 (1) (1999) 82.
- [7] A. Saad, S.J. Ludtke, J. Jakana, F.J. Rixon, H. Tsuruta, W. Chiu, *J. Struct. Biol.* 133 (1) (2001) 32.
- [8] J. Zhu, P.A. Penczek, R. Schroder, J. Frank, *J. Struct. Biol.* 118 (3) (1997) 197.
- [9] R. Henderson, J.M. Baldwin, K.H. Downing, J. Lepault, F. Zemlin, *Ultramicroscopy* 19 (1986) 147.

- [10] J. Frank, et al., *Ber. Bunsengesellschaft f. Physikalische* 74 (1970) 1105.
- [11] J.J. Fernández, J.R. Sanjurjo, J.M. Carazo, *Ultramicroscopy* 68 (1997) 267.
- [12] R.L. Kashyap, *IEEE Trans. Information Theory* IT-30 (5) (1984) 736.
- [13] W. Press, B. Flannery, et al., *Numerical Recipes in C*, Cambridge University Press, Cambridge, 1988.
- [14] M. Van Heel, B. Gowen, R. Matadeen, E.V. Orlova, R. Finn, T. Pape, D. Cohen, H. Stark, R. Schmidt, M. Schatz, A. Patwardhan, *Q. Rev. Biophys.* 33 (4) (2000) 307.